

Tuning the anomalous Hall effect of the high Curie temperature nodal-line metal Fe₃Ga via Mn doping and associated band topology


Zezhong Li,¹ Mengwei Liu,¹ Dongwei Wang,² Enke Liu,^{3,*} and Zhuhong Liu^{1,†}

¹Department of Physics, University of Science and Technology Beijing, Beijing 100083, China

²CAS Key Laboratory of Standardization and Measurement for Nanotechnology,

National Center for Nanoscience and Technology, Beijing 100190, China

³Beijing National Laboratory for Condensed Matter Physics, Institute of Physics, Chinese Academy of Sciences, Beijing 100190, China

 (Received 15 April 2024; revised 15 July 2024; accepted 5 August 2024; published 3 September 2024)

The Fe₃Ga alloy with *D*0₃ phase has been reported to exhibit remarkable anomalous transport properties arising from the topological nontrivial nodal lines. In this study, the effect of Mn doping on the magnetic, electronic, and anomalous transport properties of polycrystalline Fe_{3-x}Mn_xGa ($x = 0, 0.4, 0.6,$ and 1) are investigated. As the Mn doping level increases, the saturated magnetization at 10 K gradually decreases, while the anomalous Hall resistivity ρ_{xy}^A shows a significant increasing trend, reaching a maximum value of $7.2 \mu\Omega \text{ cm}$ in Fe₂MnGa. The analysis of anomalous Hall effect (AHE) based on the expanded scaling mechanism proposed by Tian *et al.* [Phys. Rev. Lett. **103**, 087206 (2009)] suggests that the AHE in Fe₃Ga is dominated by intrinsic mechanism, with an intrinsic anomalous Hall conductivity (σ_{xy}^{int}) of 288 S/cm. In samples with $x = 0.4$, extrinsic impurity and phonon scattering cannot be neglected and σ_{xy}^{int} decreases to 174 S/cm. As x increases to 0.6, the intrinsic mechanism vanishes and the extrinsic impurity and phonon-scattering mechanisms become dominant in the AHE. A further enhanced extrinsic scattering in the AHE is observed in Fe₂MnGa at low temperature with an anomalous Hall conductivity of 237 S/cm at 10 K. From *ab initio* calculations, we notice a σ_{xy}^{int} peak of 2310 S/cm locates approximately -0.5 eV below Fermi level (E_F) in Fe₃Ga alloy, originating from the six linked nodal rings. When one Fe atom is substituted by Mn, this peak shifts to 0.5 eV above E_F in Fe₂MnGa. We propose that partially doping Fe with Mn in Fe₃Ga may tailor the large peak of σ_{xy}^{int} around E_F .

DOI: [10.1103/PhysRevB.110.104407](https://doi.org/10.1103/PhysRevB.110.104407)

I. INTRODUCTION

Iron-rich binary alloys possess rich physical properties and have extensive applications in various fields, such as spintronics, thermoelectricity, and magnetic actuation [1–3]. In the past decades, the Fe-Ga alloys have attracted considerable attention for their magnetostriction with outstanding characteristics of low-temperature dependency and low-saturation magnetic field, having significant applications in underwater sonar and precise control of robots [4,5]. Under a suitable heat treatment, Fe-Ga alloy crystallizes into ferromagnetic *D*0₃ phase with a space group of *Fm*3̄*m* when the Ga content falls within the range of 23–26% [5–7]. Along the body diagonal, atom position of *D*0₃ phase is defined as *A* (0, 0, 0), *B* (1/4, 1/4, 1/4), *C* (1/2, 1/2, 1/2), and *D* (3/4, 3/4, 3/4), forming a body-centered cubic (bcc) structure. Very recently, it has been observed that the stoichiometric Fe₃Ga alloy with *D*0₃ phase exhibits a large anomalous Hall effect (AHE) and anomalous Nernst effect (ANE) due to the large Berry curvature (BC) around the *L* point in momentum space [2]. This large BC originates mainly from a nodal web, i.e., a flatband structure

made of the interconnected nodal lines from valence- and conduction bands, when including spin-orbit coupling (SOC).

The mechanism of AHE is generally thought to involve both intrinsic and extrinsic contributions, and the topology concepts of band structures offer a profound understanding for researchers in the intrinsic mechanism. It is proposed that the intrinsic anomalous Hall conductivity (AHC) is determined by the integral of BC of the occupied Bloch states in the whole first Brillouin zone [8–10]. Alloys with band structures characterized by nonzero topological invariant are defined as nontrivial topological materials, such as Weyl nodes, Dirac nodes, and nodal lines, generating significant BC in the presence of SOC. Therefore, a large AHE can be observed in experiments when these topological band structures are located just at or very close to the Fermi level, E_F . For instance, in typical Weyl semimetals Co₃Sn₂S₂ [11] and Co₂MnGa [12], the experimental values of the AHC reach 1310 and 1530 S/cm, respectively. Our previous study showed Fe₃Ge with hexagonal structure possessed nodal lines near E_F [13], which generated the AHC of 175 S/cm at 5 K. It has been reported that the nodal planes (lines) exist in hexagonal Fe₃Sn [14], which can produce a large AHC of -500 S/cm at 200 K. Lv suggests that the cubic Fe₇₀Al₃₀ exhibits an intrinsic component of -374 S/cm originating from nodal lines around E_F [15]. The hexagonal Fe₃Sn₂ hosts an intrinsic AHC component of about 200 S/cm above room temperature associated

*Contact author: eklui@iphy.ac.cn

†Contact author: zhliu@ustb.edu.cn

with the Dirac bands [16]. The extrinsic mechanism of AHE comprises two scattering types: the skew scattering [17,18] and the side jump [19], both of which involve the scattering of conducting electrons by the impurity under SOC. Doping with a new element may influence both the intrinsic band-topology property and the extrinsic scattering process, leading to changes in the contributions of extrinsic and intrinsic mechanisms to the AHE. For instance, in single-crystal $\text{Co}_{1-x}\text{Fe}_x\text{S}_2$ with $x = 0.05$, the experimental AHC reaches 2500 S/cm, significantly larger than that of CoS_2 [20]. The calculation suggests that the improvement of AHC is attributed to the tuning of E_F to four BC hotspots, namely Dirac point, resulting from doping with Fe. Partially replacing Co with Fe element in $\text{Co}_3\text{Sn}_2\text{S}_2$ can increase the AHC from 1310 to 1800 S/cm by enhancing extrinsic scattering contribution while maintaining the band topology [21]. In Heusler alloy $\text{MnPt}_{1-x}\text{Ir}_x\text{Sn}$, the dominant component of AHE shifts from extrinsic to intrinsic as the doping content x increases from 0 to 0.5 [22]. Yang *et al.* have reported a transition from intrinsic to extrinsic mechanism in $\text{PrAlGe}_{1-x}\text{Si}_x$ when $x > 0.5$ [23].

Substituting Fe_3Ga alloy with a different transition element can lead to various electronic and magnetic properties, making it a topic worthy of investigation. Seema *et al.* suggest that Fe_2CoGa alloy, with Co substitution, demonstrates half metallicity with 100% spin polarization [24]. It has been reported that face-centered cubic (fcc)- Fe_2MnGa with $L1_2$ phase undergoes a ferromagnetic to antiferromagnetic transition [25] as well as an obvious exchange-bias effect [26]. Our previous research studied the complex phase evolution of Mn-doped Fe in Fe_3Ga under different annealing conditions [27]. Azar *et al.* reported that in $\text{Fe}_{3-x}\text{Mn}_x\text{Z}$ ($Z = \text{Al}, \text{Ge}, \text{and Sb}$) Heusler alloys, the introduction of Mn atoms led to a reduction in the magnetic moment of Fe atoms, and resulted in significant decrease in the total magnetic moment [28]. This reduction in atomic moment weakened the exchange splitting between two spin channels, and caused the movement of E_F in both spin channels. This provided a way to tune the E_F position and to study the related physical properties in a ferromagnetic material. However, anomalous transport properties of $\text{Fe}_{3-x}\text{Mn}_x\text{Ga}$ have not been studied in the literature. Therefore, in this work, we experimentally and theoretically investigated the effect of Mn doping on the magnetic, electronic, and anomalous transport properties in $\text{Fe}_{3-x}\text{Mn}_x\text{Ga}$ ($x = 0, 0.4, 0.6, \text{ and } 1$) alloys. Furthermore, from *ab initio* calculation, we focused on a large peak of σ_{xy}^{int} below E_F in Fe_3Ga alloy, which shifted to above E_F in Fe_2MnGa alloy. We propose that partially doping with Mn atom in Fe_3Ga alloy could be a way to tune the peak of σ_{xy}^{int} toward E_F .

II. EXPERIMENTS AND CALCULATION

Bulk materials $\text{Fe}_{3-x}\text{Mn}_x\text{Ga}$ ($x = 0, 0.4, 0.6, \text{ and } 1$) were prepared by traditional arc melting from high-purity elements in an ultrahigh-purity argon atmosphere. Each sample was flipped and remelted several times to achieve good chemical homogeneity. The obtained ingots were annealed under different conditions. The Fe_3Ga alloy was quenched at 1073 K after 3 days of annealing, while samples with $x = 0.4$ and 0.6 quenched at 623 K also following 3 days of annealing. The Fe_2MnGa sample was not subjected to heat treatment.

All samples were characterized by x-ray-diffraction (XRD) technique using a Rigaku Smartlab3 instrument with $\text{Cu-K}\alpha$ source, and all samples exhibited bcc structure (see Fig. S1 in Supplemental Material [29]). The transport and magnetic properties measurement were carried out using the Quantum Design Physical Properties Measurement System. The polycrystalline samples were cut into rectangular sheets and milled into a thin slice with the thickness of $\sim 150 \mu\text{m}$. Both the transport and magnetic properties were measured on the same sample with the magnetic field perpendicular to the slice surface. The six-probe method was used for the longitudinal and Hall resistivity measurements.

To investigate the electronic property of stoichiometric $\text{Fe}_{3-x}\text{Mn}_x\text{Ga}$, the Vienna *Ab initio* Simulation Package (VASP) [30] based on a density-functional theory was employed. The exchange-correlation interaction was described by the generalized gradient approximation [31] of Perdew-Burke-Ernzerhof [32]. To achieve good convergence, the plane-wave cutoff energy was set to 500 eV and the self-consistent field was 10^{-7} eV. We projected the Bloch wave functions into a maximally localized Wannier function and constructed a tight-binding model Hamiltonian. We considered the d orbitals of Fe and Mn atoms, as well as s and p orbitals of Ga atom to obtain the Wannier functions. By employing this model, we evaluated the intrinsic AHC and BC using WANNIER90 [33] and WANNIERTOOLS [34].

III. RESULTS AND DISCUSSION

The parent alloy Fe_3Ga was demonstrated as a pure $D0_3$ phase after being annealed at 800 °C, as depicted in the inset of Fig. 1(a). Through doping, Mn atoms tended to substitute Fe atoms in the B site and the samples $\text{Fe}_{3-x}\text{Mn}_x\text{Ga}$ with $x = 0.4, 0.6, \text{ and } 1$ maintained the bcc structure like Fe_3Ga . Figure 1(a) shows the longitudinal resistivity ρ_{xx} as a function of temperature from 350 to 10 K. Obviously, the residual resistivity ρ_{xx0} of the samples monotonically increased from 14 to 174 $\mu\Omega \text{ cm}$ as x increased from 0 to 1, indicating the increased scattering effect of Mn doping on carriers. Each sample exhibited a positive temperature coefficient of resistance (TCR), indicating metallic behavior, while the TCR gradually decreased with Mn doping. The residual resistivity ratio (RRR) was defined as $\rho_{300 \text{ K}}/\rho_{10 \text{ K}}$. In general, materials with higher RRR values signify higher purity and fewer impurities. In Fe_3Ga , the RRR was 7.57, and the squarelike variation of ρ_{xx} at low temperatures ($T < 100 \text{ K}$) indicated that electron-magnon scattering played a significant role. The RRR gradually decreased to 1.39, 1.24, and 1.06 for samples with $x = 0.4, 0.6, \text{ and } 1$, respectively. This decrease in RRR was attributed to the introduction of Mn atoms as the impurities. Notably, the increase in ρ_{xx} of Fe_2MnGa was significantly smaller than that of the other three samples. In fact, the ρ_{xx} of the sample with $x = 0.6$ even surpassed that of Fe_2MnGa in high-temperature range. The pseudogap at E_F of Fe_2MnGa in spin-down channel [see Fig. 5(d)] suggested the localization of electrons, which might have been the reason for the lower TCR in Fe_2MnGa . On the other hand, since fcc- Fe_2MnGa exhibited a negative TCR (see Fig. S2 in Supplemental Material [29]), the small amount of fcc- Fe_2MnGa

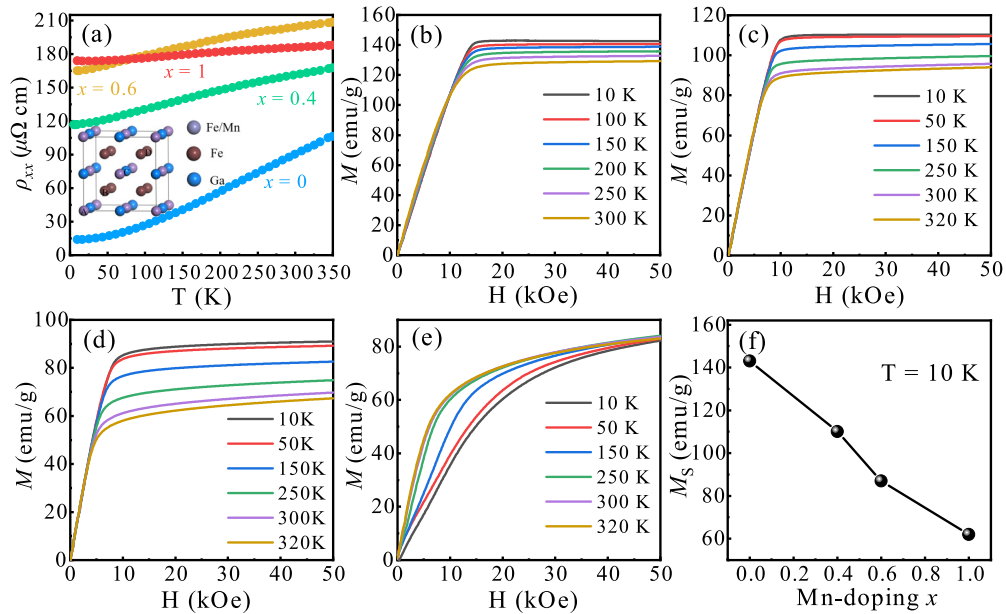


FIG. 1. (a) Temperature dependence of the longitudinal resistivity ρ_{xx} for $\text{Fe}_{3-x}\text{Mn}_x\text{Ga}$ ($x = 0, 0.4, 0.6,$ and 1), and the inset shows the diagram of crystal structure for DO_3 and $L2_1$ phase. Magnetic-field dependence of magnetization at different temperatures for $\text{Fe}_{3-x}\text{Mn}_x\text{Ga}$ with (b) $x = 0$, (c) $x = 0.4$, (d) $x = 0.6$, and (e) $x = 1$. (f) The saturated magnetization was at 10 K for all samples.

impurity could have also contributed to the reduction of the TCR in the Fe_2MnGa sample.

Figures 1(b)–1(e) show the initial magnetization curves measured at different temperatures. It is evident that all the samples exhibited a saturation behavior within 15 kOe, and the saturation magnetization (M_S) could be obtained as the intercept by linearly extrapolating from the saturated data to zero field. In Fe_3Ga alloy [Fig. 1(b)], the maximum M_S reached 143 emu/g ($6.077 \mu_B/\text{f.u.}$, where f.u. is formula units), at a low temperature of 10 K. The M_S showed a slight decrease as the temperature increased, indicating the Curie temperature (T_C) was well above 300 K, consistent with the previous study that the T_C of Fe_3Ga was 720 K [35]. In sample with $x = 0.4$, due to the introduction of Mn-Fe antiferromagnetic coupling, the value of M_S decreased to 110 emu/g at 10 K, which corresponded to $4.668 \mu_B/\text{f.u.}$, as shown in Fig. 1(c). When doping content $x = 0.6$, the M_S at 10 K further decreased to 87 emu/g ($3.689 \mu_B/\text{f.u.}$). Furthermore, M_S decreased faster than sample with $x = 0.4$ with the increased temperature [see Fig. 1(d)]. For Fe_2MnGa sample [see Fig. 1(e)], it was found that the saturation field increased in low-temperature range, and the M_S at 10 K was 62 emu/g, which corresponded to $2.625 \mu_B/\text{f.u.}$, much smaller than those of above three samples. As our *ab initio* calculation indicated, with doping content x increased, the alloy transitioned from ferromagnet ($x = 0$) with $6.07 \mu_B/\text{f.u.}$ to ferrimagnet ($x = 1$) with $2.01 \mu_B/\text{f.u.}$, consistent with previous study [36]. The experimental value of Fe_2MnGa was higher than theoretical value $2.01 \mu_B/\text{f.u.}$. The atom disorder in the real samples was inevitable, which should be responsible for the experimental moment deviation from the theoretical calculation value. Xin *et al.* proposed that the swap disorder between Fe (A) and Mn (B) in Fe_2MnGa could significantly enhance the total moment. This enhancement was attributed to the fact that this type of disorder could be seen as an intermediate state between $L2_1$ and XA phase; the

XA phase possessed a high moment of $7.5 \mu_B/\text{f.u.}$ [36]. Go *et al.* suggested that in Cr doping $\text{Fe}_3\text{Si}_{0.5}\text{Al}_{0.5}$ alloy, a small disordered Cr occupation on A and C sites led to an increase in total magnetic moment compared with the ordered structure [37]. We did not observe any obvious Curie transition with rising temperature in Fe_2MnGa , indicating that T_C was higher than 300 K, which was quite higher than T_C of 185 K reported by Xin *et al.* [36]. It can be noticed in Fig. 1(e) that the magnetization of Fe_2MnGa sample exhibited an unsaturated characteristic at low temperatures and approached the nearly same value at 50 kOe at different temperatures, different from the other samples. To elucidate this characteristic, the hysteresis loops of magnetization were measured (see Fig. S3 in Supplemental Material for details [29]; see also Ref. [38] therein). At 10 K, the sample was difficult to saturate and reached 93 emu/g at 90 kOe. As the temperature increased, the magnetization increased more rapidly with the field but reached a lower value at 90 kOe. Consequently, the $M-H$ curves at different temperatures intersected at 54 kOe, leading to the nearly identical value at 50 kOe in Fig. 1(e). Since the fcc- Fe_2MnGa exhibited antiferromagnetic property at low temperatures, and underwent a field-driven transition to ferromagnetic at 150 K, the unsaturated characteristic of our Fe_2MnGa sample at low temperatures was attributed to the presence of a small amount of fcc- Fe_2MnGa impurity, as characterized by XRD (see Fig. S1 for details [29]). Figure 1(f) displays the M_S at 10 K, which exhibits a decreasing tendency as Mn content increases.

Figure 2 shows the Hall resistivity ρ_{xy} as the function of magnetic field at different temperatures. In sample Fe_3Ga [Fig. 2(a)], the ρ_{xy} at high field was almost close to zero at 10 K, and gradually increased as temperature rose, and reached $2.22 \mu\Omega\text{ cm}$ at 300 K. In sample with $x = 0.4$ as shown in Fig. 2(b), the high-field ρ_{xy} significantly increased to about $2.9 \mu\Omega\text{ cm}$ at 5 K, and then continued to increase as

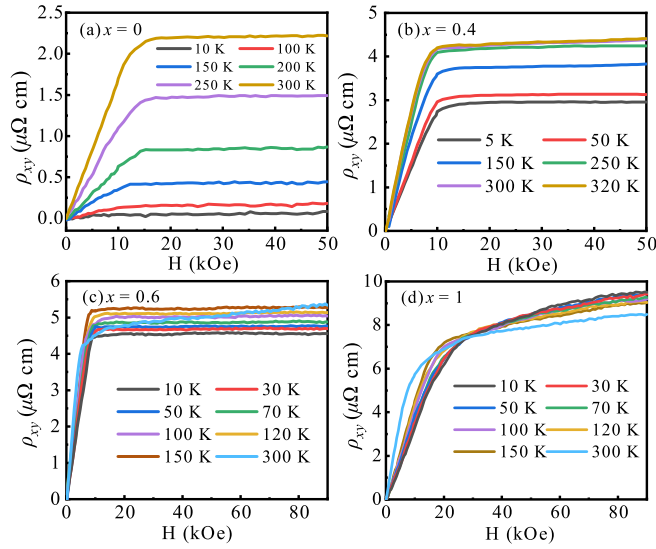


FIG. 2. (a)–(d) Magnetic-field dependence of transverse resistivity ρ_{xy} for $\text{Fe}_{3-x}\text{Mn}_x\text{Ga}$ with $x = 0, 0.4, 0.6,$ and 1 , respectively.

temperature rose. For sample with $x = 0.6$ as shown in Fig. 2(c), high-field ρ_{xy} increased to $4.6 \mu\Omega \text{ cm}$ at 10 K , and increased to the maximum of $5.3 \mu\Omega \text{ cm}$ as temperature rose to 150 K . For Fe_2MnGa ($x = 1$) shown in Fig. 2(d), the saturation field increased mildly below 150 K , which was similar to that of magnetization curve. The ρ_{xy} reached $9.5 \mu\Omega \text{ cm}$ at 90 kOe , and slightly decreased to $8.9 \mu\Omega \text{ cm}$ as temperature rose to 150 K . It is worth noting that the $\rho_{xy} - H$ curves also exhibited the similar crossing behavior as $M - H$ curves, as shown in Fig. 2(d). This is because ρ_{xy} was dependent on the magnetization. The ρ_{xy} hysteresis loops of $\text{Fe}_{3-x}\text{Mn}_x\text{Ga}$ for $x = 0.4, 0.6,$ and 1 were measured at $10, 150,$ and 300 K , as shown in Fig. S4. For samples with $x = 0.4$ and 0.6 , the ρ_{xy} exhibited no hysteresis for all temperatures, and showed the soft magnetic properties. In contrast, the ρ_{xy} of the Fe_2MnGa sample, shown in Fig. S4(c), displayed coercivity with coercive field H_C of approximately 3 kOe , consistent with the $M - H$ hysteresis loops. Notably, this hysteresis behavior disappeared when the temperature reached 300 K .

According to the empirical formula, ρ_{xy} consisted of ordinary Hall resistivity and anomalous Hall resistivity (ρ_{xy}^A), which could be written as $\rho_{xy} = \rho_{xy}^O + \rho_{xy}^A = R_0H + R_S\mu_0M$, where R_0 , R_S , and M were ordinary Hall coefficient, anomalous Hall coefficient, and the magnetization, respectively. By linearly extrapolating from the saturated data to zero field, the intercept of zero field and the slope corresponded to ρ_{xy}^A and R_0 , respectively. The ρ_{xy}^A at different temperatures for all samples are presented in Fig. 3(a). In the Fe_3Ga alloy, ρ_{xy}^A was rather small, with a value of $0.065 \mu\Omega \text{ cm}$ at 10 K , and gradually increased with temperature, which finally reached $2.2 \mu\Omega \text{ cm}$ at 300 K . ρ_{xy}^A of all samples increased with increasing Mn content at specific temperature, and reached a maximum value of $7.2 \mu\Omega \text{ cm}$ at 120 K in Fe_2MnGa . The R_0 and carrier concentration (n) were related by relationship: $R_0 = 1/ne$. The n of samples with $x = 0, 0.4,$ and 0.6 were calculated, which were on the order of 10^{23} cm^{-3} (see details in Part IV in the Supplemental Material [29]).

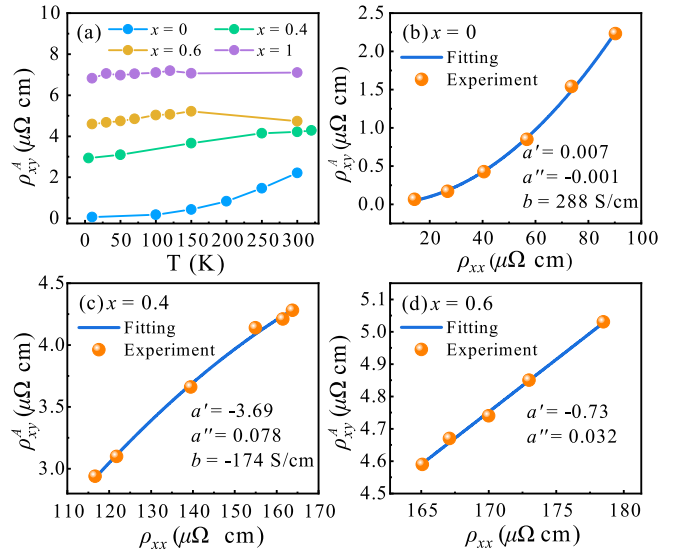


FIG. 3. (a) Temperature dependence of anomalous Hall resistivity ρ_{xy}^A . The variation of ρ_{xy}^A with ρ_{xx} and the fitting curve for (b) $x = 0$, (c) 0.4 , and (d) 0.6 .

In order to clarify the anomalous Hall contribution of different mechanisms, we plotted ρ_{xy}^A vs ρ_{xx} curves and fitted [Figs. 3(b)–3(d)] them using the expanded fitting equation proposed by Tian *et al.* [39], $\rho_{xy}^A = a'\rho_{xx0} + a''\rho_{xxT} + b\rho_{xx}^2$. Here, the $\rho_{xxT} = \rho_{xx} - \rho_{xx0}$ was the phonon-induced resistivity contribution. The parameters a' and a'' were related to impurity-induced and phonon-induced skew scattering, while parameter b represented the combined side jump and intrinsic Berry phase contribution. In Fe_3Ga , as shown in Fig. 3(b), the parameters a' , a'' , and b were 0.007 , -0.001 , and 288 S/cm , respectively, where the near-zero a' and a'' indicated the negligible corresponding skew-scattering contribution. The side-jump contribution could be estimated by $(e^2/h\alpha)(\epsilon_{\text{SO}}/E_F)$, where h , α , and ϵ_{SO} were, respectively, Planck constant, lattice constant, and spin-orbit interaction. Generally, in ferromagnetic Heusler alloys, this evaluated contribution was too low to be considered [13,40,41], and thus, we assumed the value of side-jump contribution negligible. Therefore, the intrinsic mechanism was about 288 S/cm . This value was smaller than that of the single-crystal Fe_3Ga of $\sim 600 \text{ S/cm}$ at low temperature [2]. This difference was attributed to impurities or disorder present in our polycrystalline sample. As for sample with $x = 0.4$, the fitted a' and a'' increased to -3.69 and 0.078 , respectively, which were much larger than that of Fe_3Ga , and indicated the increasing contribution of extrinsic skew scattering to the AHE in Mn doping sample. The parameter b of -174 S/cm indicated that the intrinsic component of AHE decreased compared with that of Fe_3Ga . In sample with $x = 0.6$, the ρ_{xy}^A increased first and gradually decreased as temperature rose to 300 K , as can be seen in Fig. 3(a). This nonmonotonicity was caused by the decrease of M_S with temperature increased. To eliminate the temperature effect of varying M_S on ρ_{xy}^A in sample with $x = 0.6$, we used the data below 100 K to evaluate the contribution of AHE, as shown in Fig. 3(d). We found that the linear variation relation became more significant and fit well

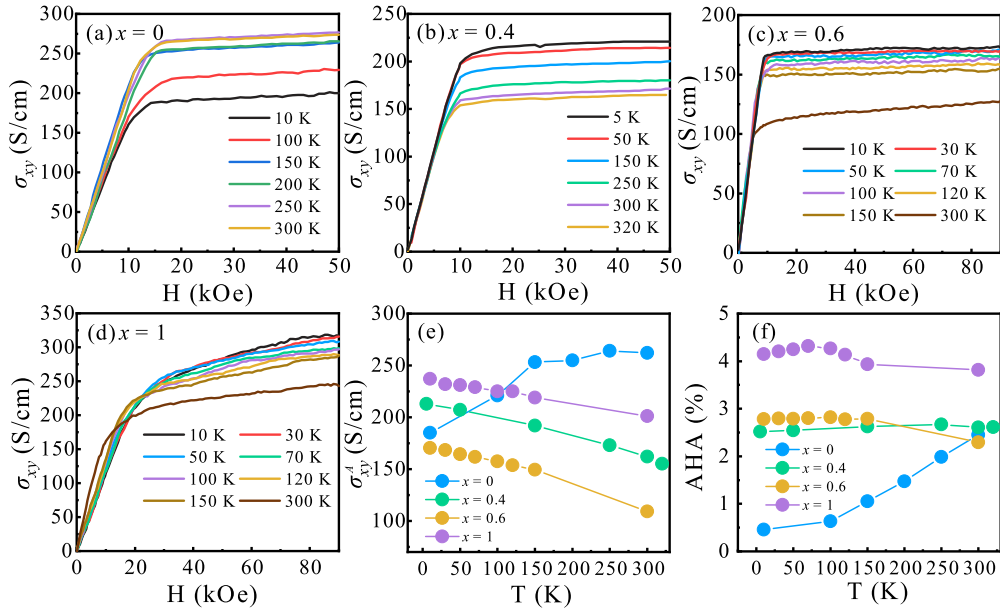


FIG. 4. (a)–(d) Magnetic-field dependence Hall conductivity σ_{xy} of $\text{Fe}_{3-x}\text{Mn}_x\text{Ga}$ with $x = 0, 0.4, 0.6$, and 1 . Temperature dependence of (e) anomalous Hall conductivity σ_{xy}^A and (f) anomalous Hall angle.

without quadratic term for sample with $x = 0.6$, expressed as $\rho_{xy}^A = a' \rho_{xx0} + a'' \rho_{xxT}$. The fitted coefficients a' and a'' were -0.73 and 0.032 , respectively, which indicated that the extrinsic skew-scattering mechanism was absolutely dominant in sample with $x = 0.6$. In both samples with $x = 0.4$ and 0.6 , the a'' was obviously higher than that of Fe_3Ga sample, which indicated the more intensive phonon-induced skew scattering. The mechanism of AHE shifted from intrinsic to extrinsic as the Mn content x changed from 0 to 0.6 . In Fe_2MnGa sample as shown in Fig. 3(a), the ρ_{xy}^A remained relatively constant as the temperature increased, which was attributed to the small variation range of ρ_{xx} with the low TCR of 1.06 . In this case, the fitted coefficients were changing strongly, resulting in unreasonable values. Therefore, fitting was not performed for the Fe_2MnGa sample.

The Hall conductivity (σ_{xy}) can be determined by the formula $\sigma_{xy} = \rho_{xy}/(\rho_{xx}^2 + \rho_{xy}^2)$, and the magnetic-field dependence of σ_{xy} is shown in Fig. 4. Extrapolating the high-field data to zero field, we could obtain the intercept as the value of AHC (σ_{xy}^A). Figure 4(e) shows temperature dependence of σ_{xy}^A for all samples. In Fe_3Ga alloy, it was observed that σ_{xy}^A increased gradually from 194 to 252 S/cm with the temperature increased from 10 to 150 K, and nearly stabilized at temperatures exceeding 150 K. However, sample with $x = 0.4$ demonstrated different behavior; σ_{xy}^A achieved the maximum value of 212 S/cm at 5 K and gradually decreased to 156 S/cm as the temperature increased to 320 K. In sample with $x = 0.6$, σ_{xy}^A was 170 S/cm at 10 K, and then decreased to 108 S/cm as temperature increased to 300 K, and exhibited the same change tendency with temperature as $x = 0.4$. In Fe_2MnGa sample, the σ_{xy}^A was 237 S/cm at 10 K, and decreased to 200 S/cm as temperature increased to 300 K, and showed the same decreasing tendency with samples $x = 0.4$ and 0.6 . Our calculation shown in Fig. 5(f) indicated that the σ_{xy}^{int} for Fe_2MnGa was only

34 S/cm at E_F , due to no topological-nontrivial band structure present. This low calculated intrinsic value indicated that the experimentally observed AHE in Fe_2MnGa also mainly originated from extrinsic mechanisms. Thus, the extrinsic scattering intensity of Fe_2MnGa was stronger than that of sample with $x = 0.6$, and led to the enhancement of AHC at 10 K from 170 to 237 S/cm, and x increased from 0.6 to 1 .

Anomalous Hall angle (AHA) was defined as $\sigma_{xy}^A/\sigma_{xx}$, and reflected the efficiency of converting longitudinal current into transverse current. Figure 4(f) shows the AHA of all samples. The Fe_3Ga alloy exhibited a modest AHA of approximately 0.5% at 10 K, due to its low longitudinal resistivity. As the temperature increased, AHA gradually increased to around 2.5% at room temperature. For samples with $x = 0.4$ and 0.6 , the AHA fluctuated between 2 and 3% , which showed slight decreasing tendency above room temperature of 300 K. In the Fe_2MnGa sample, the AHA was notably enhanced to over 3.5% across the entire temperature range, and reached 4.3% at 70 K. While not extremely high, this value was comparable to many alloys in the literature. For instance, the AHA of Mn_3Sn was reported to be 3.2% [42], 1.1% for Fe_3Sn_2 [16], 1.3% for Co_2FeAl [43], and 5.7% for MnGa [44].

We employed *ab initio* calculations using VASP and WANNI90 and obtained the density of states (DOS), band structures, and σ_{xy}^{int} in the studied $\text{Fe}_{3-x}\text{Mn}_x\text{Ga}$ ($x = 0$ and 1). The DOS diagram of Fe_3Ga in Fig. 5(a) shows there is an obvious exchange splitting between the two spin channels, which indicates a strong ferromagnetic configuration. The overlap of the peaks of Fe (A, C) and Fe (B) within the energy -2 to 2 eV also indicated the strong hybridization between them. The calculation showed that magnetic moment of Fe_3Ga was $6.07 \mu_B/\text{f.u.}$, with $1.91 \mu_B/\text{f.u.}$ for Fe (A, C) atom and $2.42 \mu_B/\text{f.u.}$ for Fe (B) atom. For Fe_2MnGa , as shown in Fig. 5(d), the introduction of Mn at B site causes

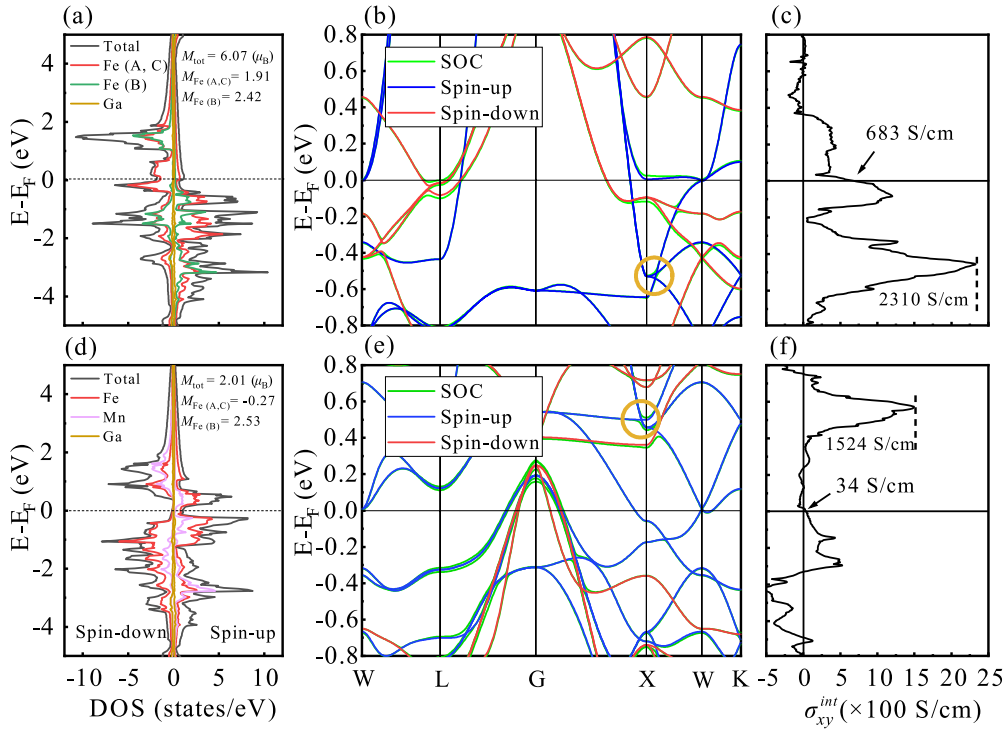


FIG. 5. Calculated total and atomic resolved density of states (DOS) for (a) Fe_3Ga and (d) Fe_2MnGa . The band structure for (b) Fe_3Ga and (e) Fe_2MnGa without SOC and with SOC. The intrinsic AHC for (c) Fe_3Ga and (f) Fe_2MnGa .

the peaks of DOS in spin-down channel to move towards the lower-energy levels, while those in the spin-up channel shift towards the higher-energy direction. This shift drastically reduced the exchange splitting and led to a reduction of magnetic moment to $2.01 \mu_B/\text{f.u.}$. Our calculations suggested that Mn atom was the primary contributor ($2.53 \mu_B/\text{f.u.}$) to the total magnetic moment in Fe_2MnGa , while the contribution of Fe ($-0.27 \mu_B/\text{f.u.}$) decreased significantly compared to that of Fe_3Ga , which formed the antiparallel magnetic-moment configuration between Mn and Fe, and indicated the ferrimagnetic property of Fe_2MnGa .

Figure 5(b) shows the band structure of Fe_3Ga , where the green line represents the band structure with SOC when the magnetization is set along z direction, while the red and blue lines represent, respectively, spin-up and spin-down bands without SOC. It was evident that a significant splitting of degenerate band occurred under the effect of SOC just below the E_F of 0.05 eV at L point. This splitting generated a large BC, resulting in a substantial σ_{xy}^{int} of 683 S/cm at E_F [see Fig. 5(c)], consistent with the previous report [2]. This value was higher than the fitted experimental intrinsic AHC of 288 S/cm , where the atomic disorder in the real samples may reduce the experimental value. In Fe_2MnGa [Fig. 5(e)], the band structure does not exhibit any topological-nontrivial property, and thus the σ_{xy}^{int} at E_F reduces to 34 S/cm [see Fig. 5(f)]. This low calculated σ_{xy}^{int} indicate that the experimentally observed AHE in Fe_2MnGa might mainly originate from an extrinsic mechanism.

In Fig. 5(c), it is worth noting that a small peak of σ_{xy}^{int} locates 0.1 eV below E_F . By slightly changing the composition of Fe_3Ga , one may tune E_F towards this peak to achieve a

larger AHC. Feng *et al.* have experimentally obtained a larger σ_{xy}^{int} of $\sim 600 \text{ S/cm}$ in $\text{Fe}_{3.09}\text{Ga}_{0.91}$ polycrystal [45], which demonstrated the feasibility of tuning the peak of σ_{xy}^{int} away from E_F towards E_F . Here, we stressed the other large peak of σ_{xy}^{int} of 2310 S/cm observed around -0.5 eV in Fe_3Ga , labeled in Fig. 5(c). This peak shifted to 0.5 eV above E_F in Fe_2MnGa . This distinct movement with doping aligned with changes in spin-up band structure. As indicated in DOS diagram, the spin-up DOS moved towards the higher-energy levels when doping content $x = 1$, implying that this shift in the peak of σ_{xy}^{int} may be attributed to the spin-up band structure. Although the theoretical calculation maximum peaks of σ_{xy}^{int} were located far away from E_F , we studied the origin of topological nontrivial band structure that generated this intrinsic AHC peak.

Without introducing SOC, the crystal structure of Fe_3Ga possesses three mirror planes of k_x , k_y , and $k_z = 0$. With the protection of time-reversal symmetry, there existed six nodal rings located in k_x , k_y , and $k_z = \pm 1$ planes, which were interconnected with each other by larger nodal lines, shown as the yellow dotted lines in Fig. 6(a). Figure 6(b) exhibits the energy gap between the nodal line-related two bands in $k_x = 1$ plane of Fe_3Ga without SOC. The details of characteristics for the band structures are exhibited in Fig. S6 in Supplemental Material [29]. It can be observed that a black ring wraps around X point, which refers to a nodal ring. When considering SOC with magnetization among z direction, the time-reversal symmetry was broken along k_x and k_y , accompanied by the broken corresponding mirror symmetry, and led nodal rings in k_x , and $k_y = \pm 1$ to gap out [shown in Fig. 6(c)], thus generated large BC. Figure 6(d) shows the band structure for Fe_3Ga along K

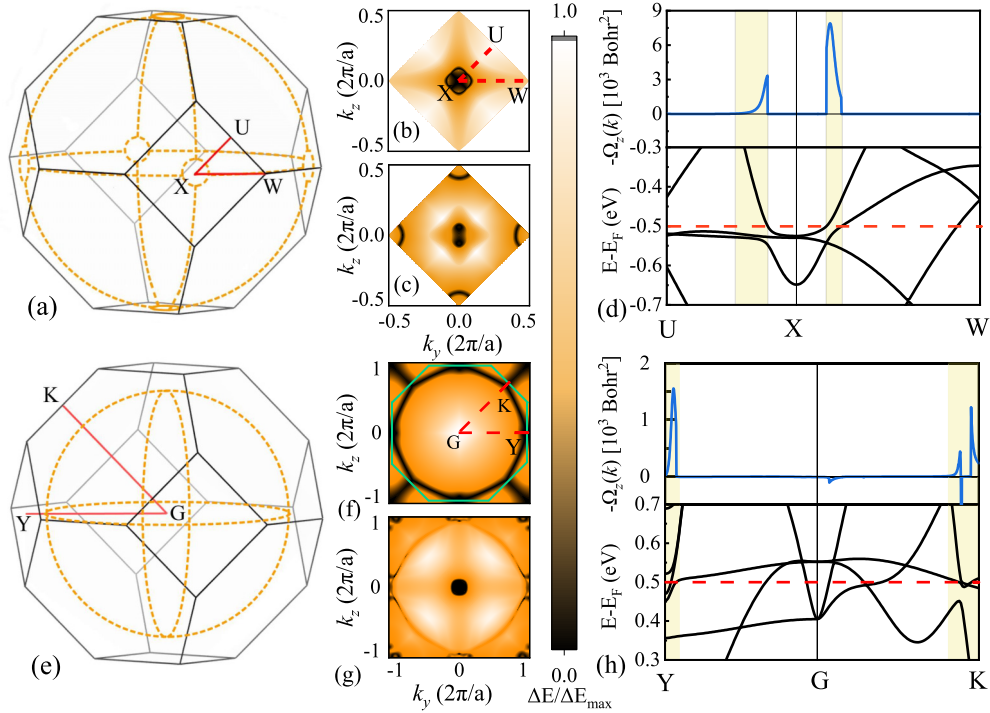


FIG. 6. (a), (e) Brillouin zone with the K -path for Fe_3Ga and Fe_2MnGa , respectively. The energy gap in $k_x = 1$ plane for Fe_3Ga (b) without SOC and (c) with SOC. The energy gap in $k_x = 0$ plane for Fe_2MnGa (f) without SOC and (g) with SOC. (d), (h) The band structure considering SOC with magnetization along z direction and the Berry curvature in z direction ($-\Omega_z$) with energy setting to -0.5 and 0.5 eV, respectively.

path of U - X - W , as well as the BC along z direction, when the energy is set to -0.5 eV. Here, we can find a not only large but also wide BC, which results in the huge intrinsic AHC peak below E_F , as labeled with dashed line in Fig. 5(c). In Fe_2MnGa , the six nodal rings merge into three larger nodal rings as shown in Fig. 6(e), moving to about 0.5 eV above E_F . The energy gap without SOC in $k_x = 0$ plane is shown in Fig. 6(f), in which the green line corresponds to the first Brillouin zone. We can identify a round nodal ring as depicted in black line, and it gaps out when we consider SOC as shown in Fig. 6(g). We perform the calculation of BC along Y - G - K path, as shown in Fig. 6(h), and it can be seen that the BC still remains large but reduces greatly compared with that of Fe_3Ga , which leads the peak of intrinsic AHC of 1524 S/cm, smaller than that of Fe_3Ga in Fig. 5. For a clearer description, we calculate the associated BC in the plane where the nodal rings exist (see Fig. S7 in Supplemental Material [29]). As the nodal rings are located 0.5 eV above E_F in Fe_2MnGa , doping a main-group element with more valence electrons than Ga (e.g., Ge, As, and Sb) may achieve a huge AHC at E_F . Noky *et al.* have theoretically indicated that a large AHC generated from three nodal lines near E_F has been suggested in Fe_2MnX ($X = \text{P}, \text{As}, \text{and Sb}$) [46], consistent with our above analysis in Fe_2MnGa . Considering the rigid model of band structure, doping partial Mn for Fe in Fe_3Ga or doping partial Mn with Fe in Fe_2MnGa , the intermediate doping composition could move the nodal line and the corresponding large intrinsic AHC peak close to the E_F . However, our experiment showed a decrease in intrinsic AHC for both $x = 0.4$ and 0.6

in $\text{Fe}_{3-x}\text{Mn}_x\text{Ga}$, and failed to obtain the large intrinsic AHC peak. This might have been due to the destruction of the nodal line arising from the broken crystal symmetry or the disorder of the samples. Further study about the AHE of single crystal $\text{Fe}_{3-x}\text{Mn}_x\text{Ga}$ is needed in the future.

IV. CONCLUSION

In this paper we experimentally and theoretically studied the effect of doping Mn in nodal-line metal Fe_3Ga alloy from the aspect of magnetic, electronic, and anomalous transport properties. The RRR of all the samples showed positive value, and the residual resistivity gradually grew with doping Mn. The M_S of Fe_3Ga alloy was 143 emu/g at low temperature of 10 K, corresponding to 6.077 μ_B /f.u., in line with the calculation value of 6.07 μ_B /f.u. The M_S at low temperature gradually decreased with Mn doping, and in Fe_2MnGa sample, the M_S decreased to 62 emu/g (2.625 μ_B /f.u.). However, this M_S was larger than the calculated value 2.01 μ_B /f.u., which may have been induced by the disorder between Fe (A) and Mn atoms. In Fe_3Ga alloy, the ρ_{xy}^A exhibited a monotonically increasing behavior with increased temperature. With Mn doping, the ρ_{xy}^A increased in the whole temperature range, and reached the maximum value of 7.2 $\mu\Omega$ cm in Fe_2MnGa at 120 K. We determined the intrinsic AHC component of Fe_3Ga sample to be 288 S/cm, which was dominant mechanism in the AHE. In sample with $x = 0.4$, the intrinsic AHC component decreased to -174 S/cm, while the extrinsic contributions from impurity and phonon scattering became non-negligible. In sample

with $x = 0.6$, the extrinsic mechanism was determined to absolutely dominate in AHE. The major mechanism in AHE shifted from intrinsic to extrinsic as x increased from 0 to 0.6. In both samples with $x = 0.4$ and 0.6, the more intensive phonon-induced skew scattering was observed compared to Fe_3Ga sample. In Fe_2MnGa sample, the σ_{xy}^A was 237 S/cm at 10 K, which was higher than all the other three samples. This enhancement was mainly induced by the extrinsic scattering procedure. *Ab initio* calculations showed a large peak of σ_{xy}^{int} around -0.5 eV below E_F in Fe_3Ga , originated from six interconnected nodal rings. This large peak was calculated to move to 0.5 eV above E_F in Fe_2MnGa alloy, and the associated nodal rings merged into three larger nodal rings.

In our experiments, the samples with $x = 0.4$ and 0.6 failed to achieve the large AHC, which may have been due to the broken crystal symmetry or the disorder and impurity in the samples. Thus, improving the quality of the samples or preparing single crystal may realize a large AHC as predicted by this calculation.

ACKNOWLEDGMENTS

This work is financially supported by National Key R&D Program of China (Grant No. 2022YFA1403400) and National Natural Science Foundation of China (Grant No. 52271164).

-
- [1] Y. Ando, K. Ichiba, S. Yamada, E. Shikoh, T. Shinjo, K. Hamaya, and M. Shiraishi, Giant enhancement of spin pumping efficiency using Fe_3Si ferromagnet, *Phys. Rev. B* **88**, 140406(R) (2013).
- [2] A. Sakai, S. Minami, T. Koretsune, T. Chen, T. Higo, Y. Wang, T. Nomoto, M. Hirayama, S. Miwa, D. Nishio-Hamane, F. Ishii, R. Arita, and S. Nakatsuji, Iron-based binary ferromagnets for transverse thermoelectric conversion, *Nature (London)* **581**, 53 (2020).
- [3] C. Shen, I. Samathrakris, K. Hu, H.K. Singh, N. Fortunato, H. Liu, O. Gutfleisch, and H. Zhang, Thermodynamical and topological properties of metastable Fe_3Sn , *npj Comput. Mater.* **8**, 248 (2022).
- [4] A. E. Clark, M. Wun-Fogle, J. B. Restorff, T. A. Lograsso, and J. R. Cullen, Effect of quenching on the magnetostriction on $\text{Fe}_{1-x}\text{Ga}_x$ ($0.13 < x < 0.21$), *IEEE Trans. Magn.* **37**, 2678 (2001).
- [5] Q. Xing, Y. Du, R. J. McQueeney, and T. A. Lograsso, Structural investigations of Fe-Ga alloys: Phase relations and magnetostrictive behavior, *Acta Mater.* **56**, 4536 (2008).
- [6] M. Matyunina, M. Zagrebin, V. Sokolovskiy, and V. Buchelnikov, *Ab initio* study of magnetic and structural properties of Fe-Ga alloys, *EPJ Web Conf.* **185**, 04013 (2018).
- [7] O. K. Goldbeck, *IRON-Binary Phase Diagrams* (Springer, Berlin, 1982).
- [8] R. Karplus and J. M. Luttinger, Hall effect in ferromagnetics, *Phys. Rev.* **95**, 1154 (1954).
- [9] G. Sundaram and Q. Niu, Wave-packet dynamics in slowly perturbed crystals: Gradient corrections and Berry-phase effects, *Phys. Rev. B* **59**, 14915 (1999).
- [10] T. Jungwirth, Q. Niu, and A. H. MacDonald, Anomalous Hall effect in ferromagnetic semiconductors, *Phys. Rev. Lett.* **88**, 207208 (2002).
- [11] E. K. Liu, Y. Sun, N. Kumar, L. Muechler, A. L. Sun, L. Jiao, S. Y. Yang, D. F. Liu, A. J. Liang, Q. N. Xu, J. Kroder, V. Süß, H. Borrmann, C. Shekhar, Z. S. Wang, C. Y. Xi, W. H. Wang, W. Schnelle, S. Wirth, Y. L. Chen *et al.*, Giant anomalous Hall effect in a ferromagnetic kagome-lattice semimetal, *Nat. Phys.* **14**, 1125 (2018).
- [12] I. Belopolski, K. Manna, D. S. Sanchez, G. Chang, B. Ernst, J. Yin, S. S. Zhang, T. Cochran, N. Shumiya, H. Zheng, B. Singh, G. Bian, D. Multer, M. Litskevich, X. Zhou, S. M. Huang, B. Wang, T. R. Chang, S. Y. Xu, A. Bansil *et al.*, Discovery of topological Weyl fermion lines and drumhead surface states in a room temperature magnet, *Science* **365**, 1278 (2019).
- [13] Z. Li, Y. B. Wang, Z. H. Xia, Q. Q. Zhang, Z. Z. Li, E. K. Liu, and Z. H. Liu, Anomalous Hall effect dominated by intrinsic mechanism in Fe_3Ge with hexagonal DO_{19} Kagome lattice and cubic DO_3 structure, *Appl. Phys. Lett.* **122**, 32401 (2023).
- [14] T. S. Chen, S. Minami, A. Sakai, Y. M. Wang, Z. L. Feng, T. Nomoto, M. Hirayama, R. Ishii, T. Koretsune, R. Arita, and S. Nakatsuji, Large anomalous Nernst effect and nodal plane in an iron-based kagome ferromagnet, *Sci. Adv.* **8**, eabk1480 (2022).
- [15] B. Lv, P. Liu, Y. Z. Wang, C. X. Gao, and M. S. Si, A large anomalous Hall conductivity induced by Weyl nodal lines in $\text{Fe}_{70}\text{Al}_{30}$, *Appl. Phys. Lett.* **121**, 072405 (2022).
- [16] L. Ye, M. Kang, J. Liu, F. von Cube, C. R. Wicker, T. Suzuki, C. Jozwiak, A. Bostwick, E. Rotenberg, D. C. Bell, L. Fu, R. Comin, and J. G. Checkelsky, Massive Dirac fermions in a ferromagnetic kagome metal, *Nature*. **555**, 638 (2018).
- [17] J. Smit, The spontaneous Hall effect in ferromagnetics I, *Physica* **21**, 877 (1955).
- [18] J. Smit, The spontaneous Hall effect in ferromagnetics II, *Physica* **24**, 39 (1958).
- [19] L. Berger, Side-jump mechanism for the Hall effect of ferromagnets, *Phys. Rev. B* **2**, 4559 (1970).
- [20] J. Choi, J. H. Park, W. Kyung, Y. Kim, M. K. Kim, J. Kwon, C. Kim, J. W. Rhim, S. Y. Park, and Y. Jo, Tunable colossal anomalous Hall conductivity in half-metallic material induced by d-wave-like spin-orbit gap, *Adv. Sci.* **11**, e2307288 (2024).
- [21] J. L. Shen, Q. Q. Zeng, S. Zhang, H. Y. Sun, Q. S. Yao, X. K. Xi, W. H. Wang, G. H. Wu, B. G. Shen, Q. H. Liu, and E. K. Liu, 33% Giant anomalous Hall current driven by both intrinsic and extrinsic contributions in magnetic Weyl semimetal $\text{Co}_3\text{Sn}_2\text{S}_2$, *Adv. Funct. Mater.* **30**, 2000830 (2020).
- [22] S. Jamaluddin, R. Roy, A. Das, S. Kanungo, and A. K. Nayak, Extrinsic to intrinsic mechanism crossover of anomalous Hall effect in the Ir-doped MnPtSn Heusler system, *Phys. Rev. B* **106**, 184424 (2022).
- [23] H. Y. Yang, B. Singh, B. Lu, C. Y. Huang, F. Bahrami, W. C. Chiu, D. Graf, S. M. Huang, B. Wang, H. Lin, D. Torchinsky, A. Bansil, and F. Tafti, Transition from intrinsic to extrinsic anomalous Hall effect in the ferromagnetic Weyl semimetal $\text{PrAlGe}_{1-x}\text{Si}_x$, *APL Mater.* **8**, 011111 (2020).
- [24] K. Seema and R. Kumar, An *ab-initio* study of full Heusler alloy Fe_2CoGa , *AIP Conf. Proc.* **1536**, 805 (2013).

- [25] X. D. Tang, W. H. Wang, W. Zhu, E. K. Liu, G. H. Wu, F. B. Meng, H. Y. Liu, and H. Z. Luo, Giant exchange bias based on magnetic transition in γ -Fe₂MnGa melt-spun ribbons, *Appl. Phys. Lett.* **97**, 242513 (2010).
- [26] E. C. Passamani, C. Larica, G. Viali, J. R. Andrez, A. Y. Takeuchi, V. P. Nascimento, V. Rodriguez, C. Rojas-Ayala, and E. Baggio-Saitovitch, In γ -Fe₂MnGa Heusler alloy do Fe and Mn sublattices magnetically couple parallel or antiparallel at low temperatures?, *J. Alloys Compd.* **628**, 164 (2015).
- [27] N. Wang, Y. Li, Z. Li, Z. Li, and Z. Liu, Evolution of phase structure and magnetic property with Mn content and heat treatment in Fe_{3-x}Mn_xGa alloy, *J. Magn. Magn. Mater.* **574**, 170723 (2023).
- [28] S. M. Azar, B. A. Hamad, and J. M. Khalifeh, Structural, electronic and magnetic properties of Fe_{3-x}Mn_xZ (Z = Al, Ge, Sb) Heusler alloys, *J. Magn. Magn. Mater.* **324**, 1776 (2012).
- [29] See Supplemental Material at <http://link.aps.org/supplemental/10.1103/PhysRevB.110.104407> for more information on the XRD pattern, the hysteresis loop of magnetization, the Hall coefficient, and the in-plane Berry curvature of the samples.
- [30] J. Hafner, Ab-initio simulations of materials using VASP: Density-functional theory and beyond, *J. Comput. Chem.* **29**, 2044 (2008).
- [31] J. P. Perdew and Y. Wang, Accurate and simple analytic representation of the electron-gas correlation energy, *Phys. Rev. B* **45**, 13244 (1992); **98**, 079904(E) (2018).
- [32] J. P. Perdew, K. Burke, and M. Ernzerhof, Generalized gradient approximation made simple, *Phys. Rev. Lett.* **77**, 3865 (1996); **78**, 1396(E) (1997).
- [33] G. Pizzi, V. Vitale, R. Arita, S. Blügel, F. Freimuth, G. Géranton, M. Gibertini, D. Gresch, C. Johnson, T. Koretsune, J. Ibañez-Azpiroz, H. Lee, J.-M. Lihm, D. Marchand, A. Marrazzo, Y. Mokrousov, J. I. Mustafa, Y. Nohara, Y. Nomura, L. Paulatto *et al.*, Wannier90 as a community code: New features and applications, *J. Phys.: Condens. Matter* **32**, 165902 (2020).
- [34] Q. Wu, S. Zhang, H. F. Song, M. Troyer, and A. A. Soluyanov, WannierTools: An open-source software package for novel topological materials, *Comput. Phys. Commun.* **224**, 405 (2018).
- [35] N. Kawamiya, K. Adachi, and Y. Nakamura, Magnetic properties and Mössbauer investigations of Fe-Ga alloys, *J. Phys. Soc. Jpn.* **33**, 1318 (1972).
- [36] Y. P. Xin, Y. X. Ma, H. Z. Luo, F. B. Meng, and H. Y. Liu, Magnetic properties and atomic ordering of BCC Heusler alloy Fe₂MnGa ribbons, *Phys. B: Condens. Matter* **489**, 51 (2016).
- [37] A. Go, K. Rećko, L. Dobrzyński, J. J. Milczarek, and M. Biernacka, Site preference and magnetism of Fe_{3-x}Cr_xAl_{0.5}Si_{0.5}, *J. Magn. Magn. Mater.* **324**, 2442 (2012).
- [38] H. Z. Luo, S. Liu, K. C. Sun, R. R. Gao, X. Y. Shi, and E. K. Liu, Enhancement of ferromagnetism in carbon doped Fe₂MnGa, *Intermetallics* **127**, 106971 (2020).
- [39] Y. Tian, L. Ye, and X. F. Jin, Proper scaling of the anomalous Hall effect, *Phys. Rev. Lett.* **103**, 087206 (2009).
- [40] S. Roy, R. Singha, A. Ghosh, A. Pariari, and P. Mandal, Anomalous Hall effect in the half-metallic Heusler compound Co₂TiX (X = Si, Ge), *Phys. Rev. B* **102**, 085147 (2020).
- [41] G. K. Shukla, A. K. Jena, N. Shahi, K. K. Dubey, I. Rajput, S. Baral, K. Yadav, K. Mukherjee, A. Lakhani, K. Carva, S. C. Lee, S. Bhattacharjee, and S. Singh, Atomic disorder and Berry phase driven anomalous Hall effect in a Co₂FeAl Heusler compound, *Phys. Rev. B* **105**, 035124 (2022).
- [42] S. Nakatsuji, N. Kiyohara, and T. Higo, Large anomalous Hall effect in a non-collinear antiferromagnet at room temperature, *Nature (London)* **527**, 212 (2015).
- [43] I. M. Imort, P. Thomas, G. Reiss, and A. Thomas, Anomalous Hall effect in the Co-based Heusler compounds Co₂FeSi and Co₂FeAl, *J. Appl. Phys.* **111**, 07D313 (2012).
- [44] F. Wu, E. P. Sajitha, S. Mizukami, D. Watanabe, T. Miyazaki, H. Naganuma, M. Oogane, and Y. Ando, Electrical transport properties of perpendicular magnetized Mn-Ga epitaxial films, *Appl. Phys. Lett.* **96**, 042505 (2010).
- [45] Z. L. Feng, S. Minami, S. Akamatsu, A. Sakai, T. S. Chen, D. Nishio-Hamane, and S. Nakatsuji, Giant and robust anomalous Nernst effect in a polycrystalline topological ferromagnet at room temperature, *Adv. Funct. Mater.* **32**, 2206519 (2022).
- [46] J. Noky, Q. N. Xu, C. Felser, and Y. Sun, Large anomalous Hall and Nernst effects from nodal line symmetry breaking in Fe₂MnX (X = P, As, Sb), *Phys. Rev. B* **99**, 165117 (2019).